

Helmholtz resonant cavity based metasurface for ultrasonic focusing

Cite as: J. Appl. Phys. **136**, 183101 (2024); doi: [10.1063/5.0233983](https://doi.org/10.1063/5.0233983)

Submitted: 19 August 2024 · Accepted: 23 October 2024 ·

Published Online: 8 November 2024



Shulong Hong,¹ Xiangkun Piao,² Xinya Yao,² Yuhang Fan,¹ Shuai Tang,¹ Cheng Lü,¹ Jiabao Yao,¹ Fengfeng Yao,¹ Yongyuan Jiang,^{1,3,4} Bingbing Cheng,^{2,a)} and Yanbo Pei^{1,3,4,a)}

AFFILIATIONS

¹Institute of Modern Optics, School of Physics, Harbin Institute of Technology, Harbin 150001, China

²Translational Research in Ultrasound Theranostics Laboratory, School of Biomedical Engineering and State Key Laboratory of Advanced Medical Materials and Devices, ShanghaiTech University, Shanghai 201210, China

³Key Laboratory of Micro-Nano Optoelectronic Information System of Ministry of Industry and Information Technology, Harbin Institute of Technology, Harbin 150001, China

⁴Key Laboratory of Micro-Optics and Photonic Technology of Heilongjiang Province, Harbin Institute of Technology, Harbin 150001, China

^{a)}Authors to whom correspondence should be addressed: peiyabo@hit.edu.cn and chengbb@shanghaitech.edu.cn

ABSTRACT

As a new method of acoustic focusing, metasurfaces have the advantage of achieving high-resolution focusing with compact and planar geometry in a relatively broad frequency band. Among these, the Helmholtz resonator cavity based metasurface has been widely utilized due to its superior performance. However, the research on this metamaterial has focused on the audible frequency band and it remains a challenge to apply this structure to the ultrasonic frequency band for biomedical applications. One reason is that the ultrasonic metasurfaces typically require complex and deep subwavelength microstructures, which is a great challenge to the current state-of-the-art fabrication techniques, and the other reason is that transferring metasurfaces with the conventional metal structure in air to those in water induces a significant transverse wave effect. In this study, we first designed a Helmholtz resonant cavity based metasurface working at 1.5 MHz according to the generalized Snell law, which is the frequency employed in biomedical applications. The resonant cavity unit was made of resin and air, which suppressed the transverse wave effect greatly. The makings and sparse distribution of the unit enabled the easy fabrication of the metasurface by 3D printing. Then, the focusing characteristics were investigated through numerical simulation and good focusing results were achieved, although the unit structure did not meet full phase coverage. Finally, the metasurface was fabricated, and the focusing was demonstrated experimentally. This work paves a way for the application of Helmholtz resonant cavity based metasurfaces in the biomedical ultrasound field.

© 2024 Author(s). All article content, except where otherwise noted, is licensed under a Creative Commons Attribution (CC BY) license (<https://creativecommons.org/licenses/by/4.0/>). <https://doi.org/10.1063/5.0233983>

I. INTRODUCTION

The focus of the sound energy has attracted increasing attention due to its widespread applications in fields ranging from ultrasound imaging^{1,2} to cancer treatment³ and non-destructive testing.⁴ Conventional acoustic lenses, engineered to redirect the trajectory of sonic waves, have historically relied on naturally occurring substances with distinct curvatures, inevitably leading to inherent geometrical distortions.⁵ However, the advent of acoustic metamaterials has revolutionized this field, enabling the creation of lenses with superior

refractive indices and reduced dimensions. Key components within these metamaterials include Helmholtz resonators,⁶ bifurcated configurations,⁷ and intricately folded spatial arrangements.^{8–10} Furthermore, the emergence of planar metamaterials, termed acoustic metasurfaces, featuring thicknesses below the wavelength scale, has expanded the possibilities for lens engineering.^{11–15} These metasurfaces boast an array of benefits, such as their streamlined architecture, minimal attenuation, and straightforward fabrication protocols,^{16–19} thereby propelling the field of acoustics into a new era of precision and efficiency.

23 November 2024 11:00:37

Among a series of metasurfaces, the advent of Helmholtz resonator metasurfaces signifies a paradigm shift, integrating traditional resonance theories with advanced metamaterial research. These metasurfaces exhibit an exceptional suite of capabilities: they provide meticulous frequency specificity,²⁰ high design flexibility,²¹ superior acoustic energy transduction efficiency,²² slim profiles,²³ comprehensive multifunctional integration,²⁴ dynamic tunability,²⁵ and formidable environmental resilience.²⁶ The amalgamation of these excellent functionalities renders Helmholtz resonator metasurfaces as an exceedingly propitious development within the acoustic sector, poised to redefine the landscape of sound manipulation and control.

Despite the prevalent utilization of Helmholtz resonator metasurfaces within the audible frequency spectrum, the endeavor to transpose their operation into the ultrasonic regime for medical applications engenders two formidable hurdles. The dimensional constraints of metasurface units necessitate a subwavelength configuration,²⁷ thereby rendering unit sizes on the order of micrometers in the ultrasonic domain—a requirement that greatly increases manufacturing costs. Additionally, while acoustic apparatuses in the audible range conventionally operate amidst gaseous media, employing metal or resin^{28–30} constructs, the transition to ultrasound contexts necessitates immersion in aqueous or analogous environments. Under these conditions, due to the small difference in impedance among metal, resin, and water, these structures made may significantly enhance the influence of transverse waves. This scenario complicates the extrapolation of design paradigms from the audible to the ultrasonic frequency bands, mandating a reevaluation of structural and material choices to accommodate the distinct acoustic dynamics inherent to each regime. In previous studies, researchers proposed a pentamode metamaterial. It has the characteristic of a particularly small shear modulus,³¹ thus overcoming significant transverse wave phenomena. However, the pentamode metamaterials still had the disadvantage of complex structures and difficulty in miniaturization.

In this paper, we have presented an exceptional opportunity to address these challenges in the development of metasurfaces, revealing the tremendous potential of Helmholtz resonator metasurfaces for applications in the ultrasonic realm. In this study, a focusing metasurface composed of Helmholtz resonant units was designed using generalized Snell's law. This metasurface operates resonantly at 1.5 MHz, encapsulated within an aqueous milieu—a quintessential condition for biomedical ultrasound interventions. Conventional acoustic metasurfaces, characterized by metal or resin configurations optimized for atmospheric conditions, encounter substantial impediments in the form of transverse wave interferences when transitioning to aquatic surroundings. To redress this predicament, we have devised a Helmholtz resonator metasurface, ingeniously fashioned from resin and air constituents, effectively attenuating the deleterious effects of transverse waves. Moreover, this paradigm facilitates the expeditious fabrication of the metasurface through the application of 3D printing methodologies. Employing numerical simulations, we have scrutinized the focal attributes of the conceptualized metasurface. Following this theoretical exploration, the metasurface was materialized, and through meticulous experimental validation, its focusing capabilities were substantiated, thereby affirming the pragmatic

viability of ultrasonic focusing predicated upon Helmholtz resonator metasurfaces.

II. DESIGN

The generalized Snell law was used to design the focusing metasurface.³² In this work, we adopted the form of Eq. (1) (Please refer to the [supplementary material](#) for the specific derivation process.),

$$\varphi(x) = \frac{2\pi}{\lambda} \sqrt{x^2 + f^2} + C, \quad (1)$$

where f was the preset focal length, which was specifically defined in this article as the distance from the focal point to the metasurface, and C was the constant of integration.

The designed phase profile for the focusing metasurface was realized through the Helmholtz resonant cavity unit. Conventionally, many Helmholtz resonators employed in air are fabricated from metallic materials. Nevertheless, the deployment of such resonators in aqueous environments engenders substantial transverse wave phenomena, attributable to the proximate impedances of water and metal.^{33,34} Furthermore, the microfabrication or nanofabrication of metallic constituents presents a formidable challenge and incurs substantial costs, rendering the theoretical conception and practical production of such devices' arduous endeavors. In our innovative approach, we elected to substitute metal with air for the construction of cavity walls, capitalizing on the marked impedance disparity between air and water. According to the reflection coefficient equation $r = (Z_1 - Z_0)/(Z_1 + Z_0)$ for the normal incidence at the interface between two mediums with acoustic resistances Z_0 and Z_1 , selecting air as the cavity wall could meet the requirement of the strong reflection of acoustic waves on the wall. To provide structural integrity, we selected resin as the [supplementary material](#) for our metasurface, given its impedance similar to that of the aqueous surroundings. The compatibility of resin with 3D printing technologies further streamlined the fabrication process, contributing to both ease of manufacture and economic viability. In simple terms, we have conceived an "anti" Helmholtz resonant cavity structure that inverts the functional roles traditionally assigned to solid and gaseous components within the canonical Helmholtz resonant cavity design. This novel configuration not only mitigates the aforementioned challenges but also opens new avenues for applying Helmholtz resonator metasurfaces to biomedical ultrasound applications.

The design of the Helmholtz resonant cavity unit is shown in [Fig. 1\(a\)](#). The propagation direction of ultrasound waves is from bottom to top. In this work, we set the phase of the subsurface of the metasurface to $\varphi = 0$ and use it as the reference plane for transmitting the phase in [Fig. 1\(b\)](#). The total width of unit h , wall thickness d_1 , d_2 , total length l , cavity length l_1 , and neck length l_2 are 0.98, 0.1, 0.05, 2.4, 2.2, and 0.72 mm, respectively. h_1 varies from 0.49 to 0.68 mm to adjust the phase delay and transmission coefficient of the unit. The width of the resonant cavity is $h_2 = (h - 2d_1 - 2d_2 - h_1)/2$. The black area represents air, whose density and speed of sound are $\rho_1 = 1.21 \text{ kg/m}^3$ and $c_1 = 343 \text{ m/s}$, respectively. The blue area represents the resin with density $\rho_2 = 1130 \text{ kg/m}^3$ and sound speed $c_2 = 1440 \text{ m/s}$, which are similar

23 November 2024 11:00:37

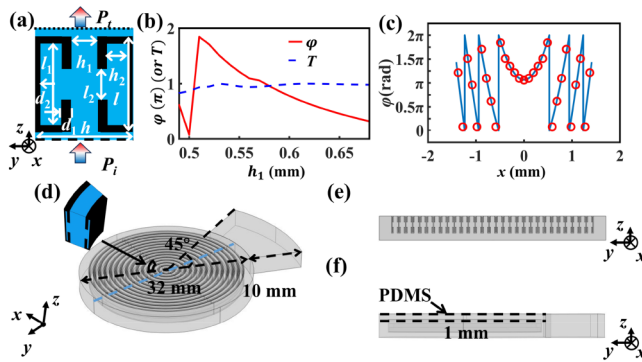


FIG. 1. (a) Structure of the designed Helmholtz resonant cavity. The arrow P_i and the dashed line indicate the direction of the incident wave and the plane at which the phase of the incident wave φ is 0. The arrow P_t and the dotted line represent the transmitted wave and its phase. (b) Transmission coefficient (T) and phase delay (φ) of the used Helmholtz resonant cavity unit as functions of the slit width h_1 . (c) Position dependent phase delay (blue line) designed by generalized Snell's law and phase delays (red circle) of Helmholtz resonant cavity units at different positions by numerical simulations. The focal length of the focusing metasurface is $f = 30$ mm. (d)–(f) Schematic diagram of the designed metasurface consisting of resin and air. (d) The 3D view of the metasurface with the PDMS layer removed and a zoom-in on one Helmholtz resonant cavity unit in the metasurface in 3D view, (e) Cut-off view of the metasurface along the blue dashed line on (d). (f) Side view of the metasurface with the PDMS layer. Note the symbols like the tail of an arrow used for the x -axis pointing inward.

to those of ambient water ($\rho_3 = 1000 \text{ kg/m}^3$, $c_3 = 1483 \text{ m/s}$). Conventionally, the size of the metasurface unit is much smaller than the wavelength. In contrast, the Helmholtz resonant cavity unit to compose the metasurface in this work is similar to the working wavelength. Therefore, adjacent discrete phase points are far apart (comparing the spacing with the wavelength of the sound wave), and the distribution is sparse.

We validated the designed Helmholtz resonator unit and focusing metasurface through the commercial finite element method solver (COMSOL Multiphysics, COMSOL Inc., Stockholm, Sweden). Considering water as the environment surrounding the designed metasurface, we used a pressure acoustic module for the simulation. The background pressure field was used to simulate the incident plane waves generated by the transducer. Plane wave radiation boundary conditions were applied to the simulation domain to prevent unnecessary reflection, and the grid size was set to be less than $\lambda_0/10$ to ensure the accuracy of simulation results.

Figure 1(b) shows the dependence of the transmittance and phase delay of the Helmholtz resonator unit on the slit width h_1 in the range from 0.49 mm to 0.68 mm. The incident ultrasound plane wave was at the frequency of 1.5 MHz (the corresponding wavelength was $\lambda_0 = 0.9887 \text{ mm}$). The results show that the transmittance is larger than 0.9 and the phase delay can cover the whole 2π range when the slit width h_1 varies from 0.49 to 0.68 mm. Therefore, the transmittance and phase delay of each unit can be adjusted to generate an ideal phase profile and construct the whole metasurface by simply changing the slit width h_1 .

In light of the dimensional limitations inherent in the 3D printing technology utilized, it is essential to guarantee that all structural parameters adhere to a threshold of no less than 0.05 mm (see detailed information of the 3D printer used in this work in the experiment). One pivotal parameter, $h_2 = (h - 2d_1 - 2d_2 - h_1)/2$, is contingent upon the slit width h_1 . As such, the operational range for h_1 in our experiments spanned from 0.49 to 0.58 mm. Obviously, this will prevent the unit from achieving full phase coverage, but it does not affect our ability to design metasurfaces using it. Please refer to the [supplementary material](#) for the specific argumentation process.

The phase profile of the metasurface, orchestrated through the application of the generalized Snell law, is graphically illustrated by the blue curve in Fig. 1(c), with a designated focal length $f = 30$ mm. The simulated phase delays of the Helmholtz resonator units distributed across distinct positions within the metasurface are symbolized by red hollow circles in the same figure. This metasurface involves taking a two-dimensional shape—obtained using the phase arrangement pattern in Fig. 1(c) and phase delay as functions of the slit width in Fig. 1(b)—and rotating it around an axis, as shown in Figs. 1(d) and 1(e). To preclude the ingress of water into the air cavities of the structure when deployed in an aquatic setting, a protective barrier consisting of a 1 mm-thick resin layer was applied to the underside of the metasurface during fabrication to ensure imperviousness. Subsequent to the 3D printing process, the upper surface was sealed with a coating of polydimethylsiloxane (PDMS). For the convenience of experimental measurement, a fan-shaped handle featuring a 45° central angle was incorporated into the metasurface design, streamlining the manipulation and positioning of the specimen throughout the experimental procedures.

III. NUMERICAL SIMULATION

The focusing efficiency of the designed structure was first established through meticulous numerical simulations. Figure 2(a) portrays the intensity distribution of the simulated acoustic pressure field within the axial plane coinciding with the ultrasonic beam axis, exhibiting a pronounced ellipsoidal focal spot. Intensity values are presented in a normalized format to enhance clarity.

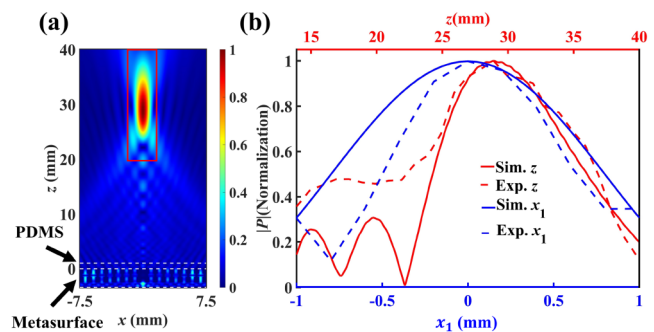


FIG. 2. (a) Simulated intensity map in the transmission domain and the location of the metasurface. (b) The profiles of normalized pressure amplitude around the focal spot along the horizontal (x_1) and vertical (z) directions of the simulation and experimental results.

A quantitative analysis of the focusing characteristics was conducted by charting the normalized intensity profiles along the orthogonal axes—vertical (z) and horizontal (x)—intersecting the focal spot, as illustrated in Fig. 2(b). The full-width at half-maximum (FWHM) for both the horizontal and vertical profiles, conventionally considered as the metric for the focal spot dimensions, was quantified to be 1.6 mm ($1.62 \lambda_0$) and 11.76 mm ($11.9 \lambda_0$), respectively. An alternative approach to determining the focal width involves measuring the interval between the proximate minima positioned on either side of the peak within the profile, yielding a horizontal width of 2.76 mm ($2.79 \lambda_0$). On the basis of the circular aperture diffraction result and the Rayleigh criterion, the diffraction-limited size of the focus can be characterized by $2.44/\lambda_0/d$, where d represents the diameter of the metasurface lens, and f represents the focal length of the metasurface lens. Within the scope of this investigation, d is measured at 28.42 mm, whereas f is specified as 30 mm. Thus, the computed diffraction-limited focal spot diameter stands at 2.54 mm ($2.58 \lambda_0$). The simulated focal width closely corresponds to the anticipated diffraction-limited dimensions. Moreover, the simulated focal length, ascertained by evaluating the distance from the metasurface to the amplitude peak, as depicted in Fig. 2(b), is determined to be 28.91 mm, aligning with the intended design parameters for the focal length. At the same time, we also used thermal-viscous acoustic modules and acoustic structure coupling modules to study the thermal viscous losses and potential acoustic structure coupling effects of the metasurface, respectively (please see the second and third sections of the [supplementary material](#)). The calculation results indicate that the impacts of these two effects can be negligible.

The effect of ultrasound resonant frequency on focusing was investigated. We found that the Helmholtz resonant cavity metasurface exhibited good focusing results at the frequency from 1.44 to 1.67 MHz. The intensity maps of the pressure field for 1.44, 1.56, and 1.67 MHz are shown in Figs. 3(a)–3(c). It was observed that the strongest point of sound pressure (i.e., the focal point) shifted further away from the metasurface with the increase in frequency. From the figure, it can be seen that in addition to the peak point (i.e., the focal point), there are many secondary intensity peaks with higher intensity, which we will simply refer to as sidelobes. These sidelobes became stronger when the frequency deviates from 1.5 MHz. Figures 3(a)–3(c) depict that the sidelobes caused by the frequency change are mainly distributed along the axial direction. For the frequencies (1.44 and 1.67 MHz), the sidelobe amplitudes were approximately 90% of the mainlobe, as shown in Fig. 3(d).

IV. EXPERIMENT

To experimentally evaluate the focusing performance of the designed metasurface, we fabricated a sample lens using a 3D printer (ProJet MJP2500, 3D SYSTEMS, USA) with Visjet M2R-WT material, whose density and sound speed are close to those used in the metasurface design and simulation. The resolution limit of the printer was $30 \mu\text{m}$. The photos of the 3D printed metasurface are shown in Fig. 4(a). The 3D printed metasurface was sealed with PDMS to isolate the air cavity from the surrounding water during the acoustic characterization. Please see the

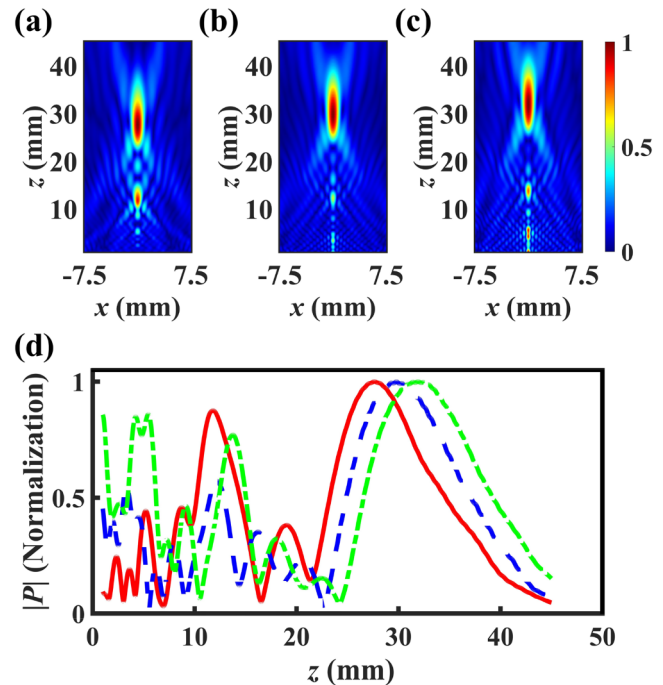


FIG. 3. (a)–(c) The simulated intensity maps of the pressure field, (a) 1.44, (b) 1.56, and (c) 1.67 MHz. (d) The profiles of normalized pressure amplitude through the focal spot along vertical (z) directions at 1.44 MHz (red line), 1.56 MHz (blue dashed line), and 1.67 MHz (green chain line).

23 November 2024 11:00:37

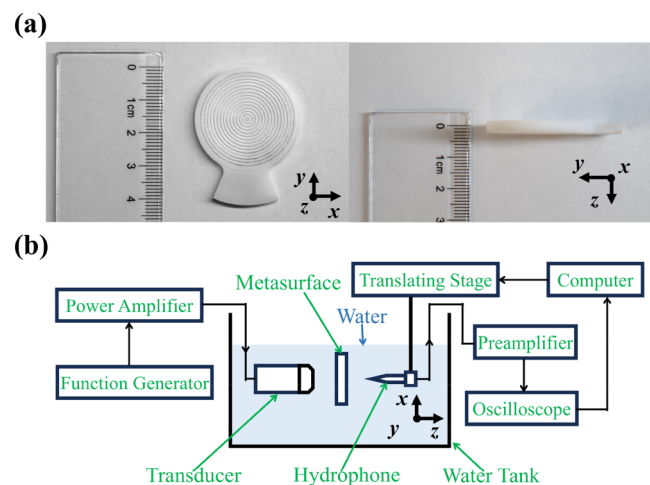


FIG. 4. (a) Photos of the 3D printed metasurface from top and side views. The PDMS layer has been removed after the measurements. (b) The diagram of the experiment setup for the acoustic field characterization. The photos of the setup are shown in the [supplementary material](#).

supplementary material for the PDMS packaging process, experimental setup, and testing process physical images.

The setup for acoustic field characterization is shown in Fig. 4(b). A planar ultrasound transducer (TP1.5P30NF, Guangzhou Doppler Electronic Technologies, China) with a center frequency of 1.5 MHz was used for generating plane waves. The transducer was driven by a function generator (33500B, Keysight Technologies, USA) and a 50-dB power amplifier (240L, Electronics & Innovation, USA). The metasurface was placed in front of the transducer. A needle hydrophone (NH0500, Precision Acoustics, UK) controlled by a 3D translation stage was used to measure the acoustic fields. The hydrophone converted the acoustic signal into the electrical signal, which was then transmitted to the oscilloscope (DSOX3012A, Keysight Technologies, USA) after passing through a preamplifier and a DC coupler. Lateral (x - y plane) and axial (x - z plane) pressure fields were measured. A raster scan with a step size of $300\ \mu\text{m}$ was performed for the acoustic field characterization in the x - y plane. The scan region was $3.6 \times 3.6\ \text{mm}^2$. A raster scan with a step size of $300\ \mu\text{m}$ in the vertical direction (x) and $200\ \mu\text{m}$ in the horizontal direction (z) was performed to obtain the acoustic field in the x - z plane. The scan region was $2.8 \times 25.2\ \text{mm}^2$. The focal length was measured from the point of maximum acoustic pressure to the metasurface.

In the experiment, we conducted measurements by placing the metasurface at distances of 10, 20, 30, 40, 50, and 60 mm from the transducer. Please see the supplementary material for the acoustic

field distribution of the six measurements. Correspondingly, the focal lengths measured are 31.4, 29.1, 31.0, 28.9, 29.1, and 28.2 mm, respectively. Based on the above data, we obtain the final focal length $29.8 \pm 1.6\ \text{mm}$, and the typical acoustic pressure fields near the focal point in the x - y and x - z planes are shown in Figs. 5(a) and 5(b). The FWHM of the horizontal and vertical profiles shown in Fig. 5(c) are 1.126 mm ($1.14\ \lambda_0$) and 14.544 mm ($14.71\ \lambda_0$), respectively. The measured and simulated results exhibit a fairly good agreement, which validate the effectiveness of the proposed metasurface lens.

V. CONCLUSION

In conclusion, we have successfully applied the Helmholtz resonator cavity metasurface into the realm of biomedical ultrasonic technology. By utilizing the generalized Snell law, we have designed an “anti” Helmholtz resonant cavity structure within a unit size that operates at the wavelength range for acoustic focusing metasurfaces. We have conducted both numerical and experimental studies on the focusing performance of the designed metasurface toward ultrasonic waves. Simulation results indicate that our proposed structure exhibits excellent focusing effects when the ultrasonic plane wave is normally incident upon the metasurface. The metasurface we printed generated focused effects at a frequency of 1.5 MHz. Given the size of the constituent units and the straightforward composition of materials (namely, air and resin), the metasurface has the distinct benefits of facile manufacturing processes and economical production. These attributes are highly advantageous for the integration of metasurfaces into ultrasonic applications. Moreover, our findings suggest that by adopting sparse structural designs, it is feasible to relax the stringent requirement for complete phase coverage in metasurface architecture, thereby substantially easing the design complexities and reducing the associated costs for fabricating ultrasonic metasurfaces. While our current exploration is confined to the development of resonant cavity metasurfaces through the application of the generalized Snell law, the conceptual framework established herein holds relevance for the broader category of phase-modulated structures, including but not limited to microporous plate metasurfaces.

SUPPLEMENTARY MATERIAL

See the supplementary material for the relevant content of the generalized Snell law, simulation results by using thermal-viscous acoustic modules and acoustic solid coupling modules, the design of metasurfaces using non-full phase coverage elements, the PDMS packaging process, experimental setup, testing process physical images, and the related acoustic field experimental data.

ACKNOWLEDGMENTS

This work was supported in part by the Fundamental Research Funds for the Central Universities (No. 2023FRFK06011), the National Natural Science Foundation of China (No. 62075048), the National Science Foundation of Shandong Province of China (No. ZR2020MF129), the Natural Science Foundation of Shanghai (No. 23ZR1442000, B.C.), and the Start-up Grant from ShanghaiTech University (No. 2021F0209-000-09, B.C.).

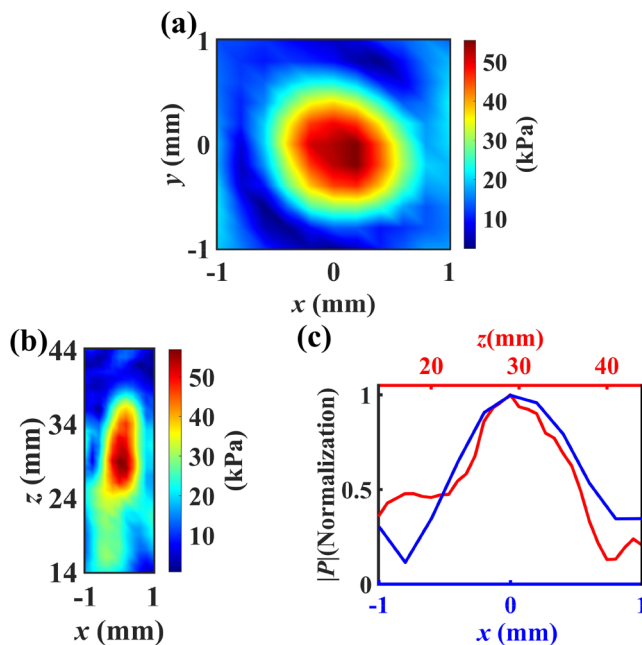


FIG. 5. (a) and (b) Images of the typical acoustic field distribution in the x - y (a) and x - z (b) planes across the focal point in the experiment. (c) Measured profiles of normalized pressure amplitude through the focal point along horizontal (x) and vertical (z) directions.

AUTHOR DECLARATIONS

Conflict of Interest

The authors have no conflicts to disclose.

Author Contributions

Shulong Hong and Xiangkun Piao contributed equally to this paper.

Shulong Hong: Conceptualization (equal); Data curation (equal); Formal analysis (equal); Methodology (equal); Software (equal); Writing – original draft (equal). **Xiangkun Piao:** Investigation (equal); Resources (equal). **Xinya Yao:** Investigation (equal); Resources (equal). **Yuhang Fan:** Data curation (equal); Formal analysis (equal). **Shuai Tang:** Conceptualization (equal); Data curation (equal); Software (equal). **Cheng Lü:** Conceptualization (equal); Data curation (equal); Software (equal). **Jiabao Yao:** Data curation (equal); Formal analysis (equal). **Fengfeng Yao:** Conceptualization (equal); Supervision (equal); Writing – original draft (equal); Writing – review & editing (equal). **Yongyuan Jiang:** Conceptualization (equal); Funding acquisition (equal); Project administration (equal); Supervision (equal). **Bingbing Cheng:** Conceptualization (equal); Project administration (equal); Supervision (equal); Writing – review & editing (equal). **Yanbo Pei:** Conceptualization (equal); Project administration (equal); Supervision (equal); Writing – review & editing (equal).

DATA AVAILABILITY

The data that support the findings of this study are available from the corresponding authors upon reasonable request.

REFERENCES

- ¹J. Li, L. Fok, X. Yin *et al.*, *Nat. Mater.* **8**, 931–934 (2009).
- ²J. P. Xia and H. X. Sun, *Appl. Phys. Lett.* **106**, 063505 (2015).
- ³J. Zhao, H. P. Ye, K. Huang, Z. N. Chen, B. W. Li, and C. W. Qiu, *Sci. Rep.* **4**, 6257 (2014).
- ⁴J. P. Xia, H. X. Sun, and S. Q. Yuan, *Sci. Rep.* **7**, 8151 (2017).
- ⁵Z. Chen, Z. Tang, and W. Wan, *Rev. Sci. Instrum.* **82**, 026103 (2011).
- ⁶J. X. Ping, X. Z. Ting, H. S. Xiang *et al.*, *Phys. Rev. Appl.* **10**, 014016 (2018).
- ⁷G. Y. Song, B. Huang, H. Y. Dong *et al.*, *Sci. Rep.* **6**, 35929 (2016).
- ⁸S. Chen, Y. Fan, F. Yang, K. Sun, Q. Fu, J. Zheng, and F. Zhang, *Front. Mater.* **8**, 790987 (2021).
- ⁹W. Q. Wang, Y. B. Xie, A. Konneker, B.-I. Popa, and S. A. Cummer, *Appl. Phys. Lett.* **105**, 101904 (2014).
- ¹⁰L. Xiang, G. X. Wang and C. Zhu, *Appl. Acoust.* **188**, 108585 (2022).
- ¹¹J. Rong and W. Ye, *Acta Mater.* **185**, 382–399 (2020).
- ¹²S. Cummer, J. Christensen, and A. Alù, *Nat. Rev. Mater.* **1**, 16001 (2016).
- ¹³X. X. Wu, X. X. Xia, J. X. Tian, Z. Y. Liu, and W. J. Wen, *Appl. Phys. Lett.* **108**, 163502 (2016).
- ¹⁴R. A. Jahdali and Y. Wu, *Appl. Phys. Lett.* **108**, 031902 (2016).
- ¹⁵S. B. Qi, Y. Li, and B. Assouar, *Phys. Rev. Appl.* **7**, 054006 (2017).
- ¹⁶H. Song, X. Ding, Z. Cui, and H. Hu, *Molecules* **26**, 4018 (2021).
- ¹⁷J. Fan, L. Zhang, S. Wei, Z. Zhang, S. Choi, B. Song, and Y. Shi, *Mater. Today* **50**, 303–328 (2021).
- ¹⁸S. Tong and C. Ren, *Appl. Phys. Lett.* **123**, 031703 (2023).
- ¹⁹Y. Bai, A. Song, and C. Sun, *Appl. Phys. Lett.* **122**, 261705 (2023).
- ²⁰Y. Zhang, H. Cheng, J. G. Tian, and S. Q. Chen, *Phys. Rev. Appl.* **14**, 064057 (2020).
- ²¹Y. Li, S. Qi, and M. B. Assouar, *New J. Phys.* **18**, 043024 (2016).
- ²²H. Liu, Y. Zheng, Y. Lu, Q. Kang, K. Guo, and Z. Guo, *Ann. Phys.* **533**, 2100218 (2021).
- ²³H. Ryoo and W. Jeon, *Int. J. Mech. Sci.* **229**, 107508 (2022).
- ²⁴Y. F. Zhu and B. Assouar, *Phys. Rev. B* **99**, 174109 (2019).
- ²⁵W. K. Cao, C. Zhang *et al.*, *Phys. Rev. Appl.* **15**, 024026 (2021).
- ²⁶B. Assouar, B. Liang, Y. Wu, Y. Li, J.-C. Cheng, and Y. Jing, *Nat. Rev. Mater.* **3**, 460–472 (2018).
- ²⁷C. Li, S. Zhang, and H. Chen, *J. Appl. Phys.* **133**, 095104 (2023).
- ²⁸C. Liu, C. Gong, H. Y. Long, Y. Gu, C. R. Ma, Y. M. Liu, Y. Z. Zhu, Y. Cheng, and X. J. Liu, *Phys. Rev. Appl.* **21**, 064043 (2024).
- ²⁹C. Shao, Y. Z. Zhu, H. Y. Long, C. Liu, Y. Cheng, and X. J. Liu, *Appl. Phys. Lett.* **120**, 083504 (2022).
- ³⁰H. Long, Y. Cheng, and X. Liu, *Sci. Rep.* **8**, 15678 (2018).
- ³¹Y. Tian, Q. Wei, Y. Cheng, Z. Xu, and X. J. Liu, *Appl. Phys. Lett.* **107**, 221906 (2015).
- ³²N. Yu, P. Genevet, M. A. Kats, F. Aieta, J.-P. Tetienne, F. Capasso, and Z. Gaburro, *Science* **334**, 333–337 (2011).
- ³³D. Ferras, P. A. Manso *et al.*, *J. Sound Vib.* **394**, 348–365 (2017).
- ³⁴A. Aladwani, A. Almandeel, and M. Nouh, *Int. J. Mech. Sci.* **152**, 151–166 (2019).